Aging and Disease
www.aginganddisease.org
Early access date: December 10, 2025
http://dx.doi.org/10.14336/AD.2025.1352

Original Article

Interthalamic Adhesion as a Potential Structural Regulator of Cerebrospinal Fluid Dynamics in the Third Ventricle

Shigeki Yamada[1, 2*], Ko Okada[3], Hirotaka Ito[3], Chifumi Iseki[4, 5], Tomoyasu Yamanaka[1], Motoki Tanikawa[1], Tomohiro Otani[6], Satoshi Ii[7], Yoshiyuki Watanabe[8], Shigeo Wada[6], Marie Oshima[2], Mitsuhito Mase[1]

[1]Department of Neurosurgery, Nagoya City University Graduate School of Medical Sciences, Aichi, Japan. [2]Interfaculty Initiative in Information Studies/Institute of Industrial Science, The University of Tokyo, Tokyo, Japan. [3]Medical System Research & Development Center, FUJIFILM Corporation, Tokyo, Japan. [4]Department of Behavioral Neurology and Cognitive Neuroscience, Tohoku University Graduate School of Medicine, Sendai, Miyagi, Japan. [5]Division of Neurology and Clinical Neuroscience, Department of Internal Medicine III, Yamagata University School of Medicine, Yamagata, Japan. [6]Department of Mechanical Science and Bioengineering, Graduate School of Engineering Science, The University of Osaka, Osaka, Japan. [7]Department of Mechanical Engineering, School of Engineering, Institute of Science Tokyo, Tokyo, Japan. [8]Department of Radiology, Shiga University of Medical Science, Shiga, Japan

[Received November 1, 2025; Revised December 7, 2025; Accepted December 8, 2025]

ABSTRACT: The interthalamic adhesion (ITA), located at the center of the brain, may influence ventricular morphology and cerebrospinal fluid (CSF) dynamics. Its role in Hakim's disease, renamed idiopathic normal pressure hydrocephalus (iNPH), remains unclear. To investigate the relationship between ITA morphology and CSF dynamics in the third ventricle using three-dimensional (3D) and four-dimensional (4D) flow MRI in healthy individuals and patients with Hakim's disease. The study participants were 83 patients with Hakim's disease (mean age, 77.0 ± 6.2 years) and 226 healthy volunteers (mean age, 58.2 ± 18.2 years) were analyzed. 3D T1-weighted MRI was used to evaluate the morphology of the third ventricle and ITA, and 4D flow MRI (velocity encoding = 5 cm/sec) was used to assess CSF streamlines and vorticity throughout the cardiac cycle. ITA width increased and ITA area decreased with third ventricle enlargement. Compared with younger healthy volunteers, older volunteers had approximately two-fold greater mean ITA width and one-third smaller mean ITA area, whereas patients with Hakim's disease had four-fold greater width and one-eighth smaller area. ITA absence was more frequent in Hakim's disease (14%) than in healthy volunteers, though this difference was not statistically significant. In healthy volunteers, downward systolic and upward diastolic streamlines with paired vortices behind the ITA were consistently observed, irrespective of age. In contrast, 63 patients with Hakim's disease (81%) lacked these flow patterns and instead exhibited abnormal bidirectional flows in the cerebral aqueduct, with some showing marked upward flow extending into the third ventricle. The ITA functions as a potential structural regulator of third-ventricular morphology and CSF dynamics. In Hakim's disease, physiological streamlines and vortices within the third ventricle are absent, and abnormal aqueductal flow predominates.

Keywords: flow dynamics, vorticity, cerebrospinal fluid, third ventricle, hydrocephalus, ventriculoperitoneal shunting, 4D flow MRI,

***Correspondence should be addressed to:** Dr. Shigeki Yamada, Department of Neurosurgery, Nagoya City University Graduate School of Medical Sciences, Mizuho-ku Nagoya, Aichi, 467-8601, Japan. E-mail address: shigekiyamada393@gmail.com.

INTRODUCTION

Since around 2012, our understanding of cerebrospinal fluid (CSF) dynamics theory may have undergone a paradigm shift [1], prompted by new insights into CSF circulation pathways. These insights have largely come from mouse models, focusing on CSF motion within a narrow region less than 1 mm beneath the cortical and meningeal surfaces [1-8]. In contrast, investigations of CSF dynamics in the human third ventricle, located deepest within the brain, remain limited, rendering the third ventricle an enigmatic central cavity of the brain. The third ventricle is anatomically surrounded by circumventricular organs [9], which can release or detect signaling molecules such as melatonin and orexin. These molecules are known to regulate the sleep–wake cycle and circadian rhythms [10-13]. Although direct CSF-mediated hormonal signaling in the third ventricle has not been definitively established, the anatomical proximity of these structures supports the hypothesis that such communication may occur via CSF flow. The mechanisms underlying these processes, however, are not yet fully elucidated.

Echocardiography has gained increasing clinical importance for the quantitative assessment of heart failure severity [14, 15]. However, the brain's enclosure within a thick and rigid skull precludes evaluation of natural CSF dynamics by ultrasound. Historically, CSF dynamics in the third ventricle were mainly studied using invasive methods in animal models [16-18]. While phase-contrast MRI has enabled noninvasive assessment in humans, its two-dimensional nature limits the detailed analysis of third-ventricular flow [19, 20]. Recent advances in MRI, including 4D flow MRI [21-25] , have enabled noninvasive three-dimensional (3D) evaluation of CSF dynamics in the human third ventricle. In our previous study using 4D flow MRI [22], we demonstrated that enlargement of the foramen of Magendie at the caudal fourth ventricle was strongly associated with increased reflux and stroke volume in the cerebral aqueduct. Nevertheless, CSF dynamics within the morphologically complex third ventricle have not been systematically characterized. We therefore applied vorticity analysis, a method applied in the evaluation of complex intracardiac blood flow [26, 27], to 4D flow MRI for assessing CSF dynamics in the third ventricle.

The interthalamic adhesion (ITA), also known as the massa intermedia, is a bridge-like structure that connects the left and right thalami across the midline. Its anatomical presence is variable, and its functional significance remains debated. A systematic review reported a higher prevalence of ITA absence in patients with schizophrenia compared with healthy individuals [28]. Similarly, a study of patients with thalamic infarction demonstrated poorer performance on verbal memory and Stroop tasks among those lacking an ITA, suggesting a potential compensatory role in interthalamic communication [29] Conversely, a histological analysis of 31 human brains identified the ITA in 51.7% of cases but found no neuronal cell bodies, concluding that it primarily consists of glial cells rather than forming a true gray commissure [30]. Further anatomical investigations reported ITA absence in 32% of males and 22% of females, with present ITAs being on average 17.5 mm² larger in females [31]. In contrast, larger MRI-based studies involving more than 200 healthy individuals reported lower absence rates (4–13%) and confirmed a significantly higher prevalence of ITA in females [32, 33].These studies also demonstrated that ITA size decreases with age and that its absence becomes more frequent in older individuals. Collectively, these findings indicate that both congenital and age-related factors may influence the presence and morphology of the ITA. Although its neuronal function remains uncertain, recent computational fluid dynamics (CFD) simulations have suggested that the ITA may affect third ventricular morphology and contribute to CSF dynamics [20, 34].

In the present study, we tested the hypothesis that the ITA is not merely a passive anatomical remnant, but a functional structure involved in maintaining the shape of the third ventricle and regulating CSF dynamics. To address this, we evaluated ITA morphology and its association with CSF flow patterns in the third ventricle using 3D T1-weighted MRI and 4D flow MRI in younger and older healthy volunteers and in patients with idiopathic normal pressure hydrocephalus (iNPH), recently renamed Hakim's disease (HD) under the new classification [35]. In this manuscript, we use the term "Hakim's disease (iNPH)" in accordance with this proposed classification, while acknowledging that it has not yet been universally adopted.

MATERIAL AND METHODS

Ethical approvals

The study design and protocol of this prospective observational study were approved by the Ethics Committees for Human Research of our institutions (IRB Number: 60-22-0083, 2022-73, R2019-227). MRI data from patients were obtained using an opt-out method after their personal information had been anonymized in a linkable manner. Healthy volunteers provided written informed consent after receiving an explanation of the study's purpose and the potential for detecting brain diseases and subsequently underwent MRI examinations. The study was conducted according to the approved guidelines of the Declaration of Helsinki.

Study population

Details of data collection, anonymization, image acquisition, and data processing methods have been described in our previous publications [22-24, 36]. In brief, this study included 30 patients diagnosed with HD (iNPH) and 133 healthy volunteers who underwent both 3D T1-weighted magnetization-prepared rapid gradient echo (MPRAGE) and 4D Flow MRI sequences on 3-Tesla MRI systems manufactured by GE Healthcare (USA) between 2019 and 2022 in one institute. In addition, 53 patients with HD (iNPH) who underwent the same sequences on 3-Tesla MRI systems manufactured by Philips (Netherlands) between 2023 and 2025 at the other institute were included. Additionally, due to the limited availability of data from healthy older adult volunteers, 93 healthy individuals aged 60 years or older who underwent the 3D T1-weighted MPRAGE sequence on a 1.5 Tesla MRI scanner made by Siemens AG (Germany), but not 4D Flow MRI, at one collaborating institution were also included for morphological analysis. Patients diagnosed with secondary normal pressure hydrocephalus or those with midlife hydrocephalus [24, 35] were excluded from this study. Twenty-five of the 83 patients with HD and 128 of the 133 healthy volunteers have been previously reported [36]. That study analyzed aqueductal and foraminal CSF flow, whereas the present work focuses on third-ventricular dynamics. In addition, 65 patients and 226 volunteers overlapped with our other study [37], which examined AI-based volumetric segmentation without ITA measurements.

Image acquisitions

The sequence parameters for 4D Flow MRI were as follows, GE: TR, variable (10–20 ms); TE, variable (3–7 ms); flip angle, 8°; FOV, 200 mm; matrix, 256 × 256; voxel size, 0.781 × 0.781 × 1.0 mm; cardiac phases, 12; VENC, 5 cm/s. Philips: TR, variable (10–20 ms); TE, variable (3–7 ms); flip angle, 8°; FOV, 200 mm; matrix, 208 × 198; voxel size, 0.89 × 0.89 × 1.0 mm; cardiac phases, 8; VENC, 5 cm/s. Images were acquired in the mid-sagittal plane over a 30 mm slab (1.0 mm × 30 slices), covering from the bilateral foramina of Monro to the upper cervical subarachnoid space. Imaging time was approximately 10 minutes, depending on heart rate, which was synchronized with peripheral pulse measurements from the finger. As the 4D Flow sequence lacked sufficient resolution in the T1-weighted magnitude images, a 3D T2-weighted fast spin-echo sequence was additionally performed to obtain anatomical details. Parameters were: TR, 2,000 ms; TE, 85.3 ms; matrix, 288 × 288; voxel size, 0.8 × 0.8 × 0.8 mm; acquisition time, ~4 minutes.

The sequence parameters for MPRAGE were as follows: repetition time (TR), 2,471 ms; time to echo (TE), 3.13 ms; inversion time, 1,000 ms; flip angle, 8°; matrix 256 × 256; voxel size, 0.9 × 0.9 × 0.9 mm; and acquisition time, approximately 4 min. The sequence parameters for Cube were as follows: TR, 2,000 ms; TE, 85.3 ms; matrix 288 × 288; voxel size, 0.8 × 0.8 × 0.8 mm; and acquisition time, approximately 4 min.

Data processing of 4D Flow MRI and automatic brain segmentation

The applications for 4D Flow MRI and brain segmentation on an independent 3D volume analyzer workstation (SYNAPSE 3D; FUJIFILM Corporation) were approved as a medical device by the Pharmaceuticals and Medical Devices Agency of Japan. The details of the 4D Flow MRI acquisition method have been described in our previous papers [22-24, 36]. In brief, the first step of 4D Flow MRI involves combining 3D velocity-encoding data obtained from triaxial phase-contrast images with morphological data of the intracranial CSF space acquired from 3D T2-weighted MRI using the 4D Flow application. In the second step, the flow velocity measurement region of 4D Flow MRI is extracted. In the third step, automated polynomial fitting is applied to correct for phase offsets, eddy currents, and background noise, ensuring accurate measurement of slow CSF flow velocities [38]. Finally, 2D and 3D flow velocity vectors, streamlines, wall shear stress, and vorticity can be visualized. The vorticity measurement technology is available only in the development version of the 4D Flow application and has not been approved as a medical device.

Using the Brain Subregion Analysis application, the intracranial spaces were segmented into 100 brain and 7 cerebrospinal fluid (CSF) subregions from 3D T1-weighted MRIs [37]. Volume ratios of the segmented brain and CSF spaces were calculated as the volume of each region divided by intracranial volume. The volume ratios of the total, third and fourth ventricles were used in this study.

Measurements of Interthalamic Adhesion

As shown in Figure 1, the area with maximum and minimum diameters of the ITA were measured on the midsagittal plane of the T1-weighted 3D MPRAGE sequence. The width of the ITA was measured on the axial plane.

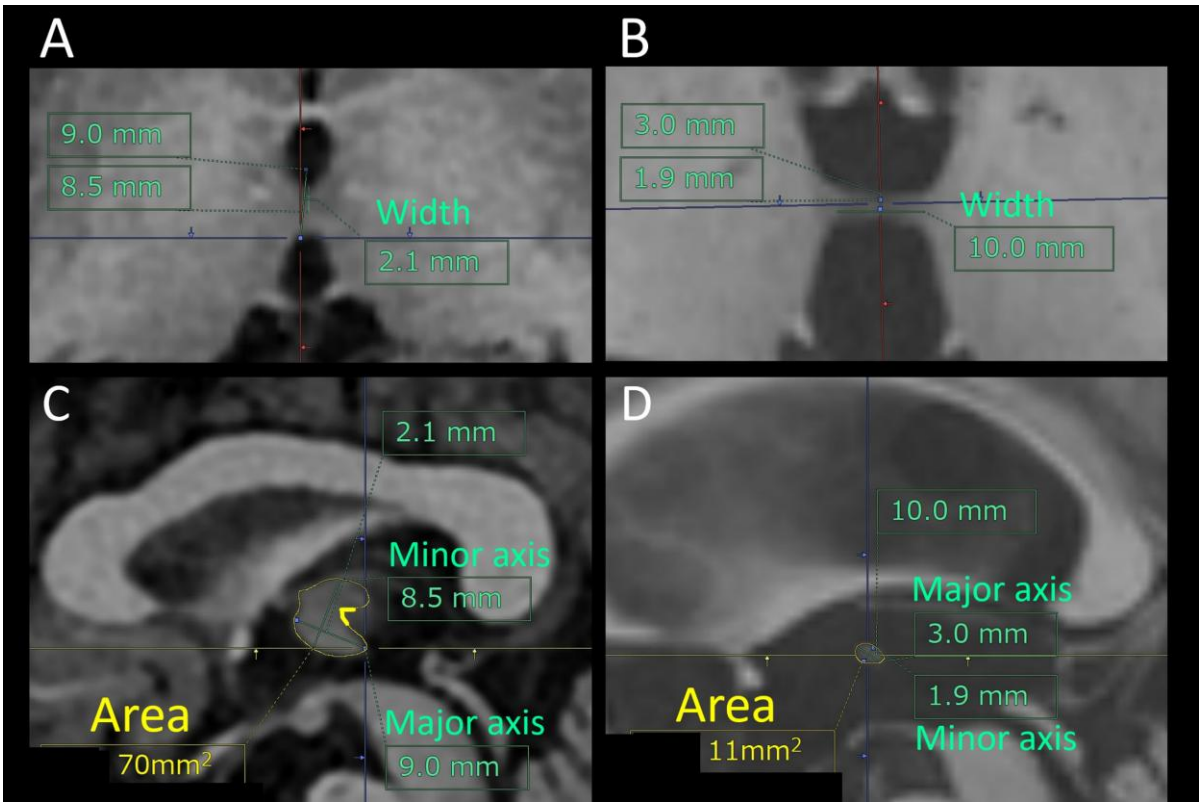

Figure 1. Measurement of the interthalamic adhesion (ITA). Representative 3D T1-weighted MR images in a healthy volunteer (A, C) and a patient with Hakim's disease (B, D). **(A and B)** Axial sections used to measure ITA width. **(C and D)** Sagittal sections used to measure ITA area, with major and minor axes indicated. The posterior recess (highlighted in yellow) is located in the ITA and extends toward the cerebral aqueduct. This structure is often visualized in healthy individuals with a prominent ITA

Vorticity Assessment Parameters

To quantify the strength of vortex flow, the vorticity $\vec{\omega}$, which represents rotational flow, is defined as follows:

$$\vec{\omega} = rot(\vec{u}) = \nabla \times \vec{u}$$

where $\vec{u}$ (u_x, u_y, u_z) represents the velocity vector at a given time and position.

The Nabla operator, ∇, is expressed as $(\partial/\partial x, \partial/\partial y, \partial/\partial z)$.

In a 3D Euclidean coordinate system, the components of the vorticity vector $\vec{\omega}$ are given by:

$$\vec{\omega} = \left(\frac{\partial u_z}{\partial y} - \frac{\partial u_y}{\partial z}, \frac{\partial u_x}{\partial z} - \frac{\partial u_z}{\partial x}, \frac{\partial u_y}{\partial x} - \frac{\partial u_x}{\partial y}\right)$$

When analyzing a 3D vortex by projecting the velocity vector onto an observed cross-section, the normal component of the vorticity vector was calculated as the rotational speed:

$$\vec{\omega} \cdot \vec{n} = n_x\left(\frac{\partial u_z}{\partial y} - \frac{\partial u_y}{\partial z}\right) + n_y\left(\frac{\partial u_x}{\partial z} - \frac{\partial u_z}{\partial x}\right) + n_z\left(\frac{\partial u_y}{\partial x} - \frac{\partial u_x}{\partial y}\right)$$

where $\vec{n}$ (n_x, n_y, n_z) represents the normal vector of the observed cross-section.

The magnitude of the normal component was maximized when the cross-section was perpendicular to the vorticity vector. The intensity of the displayed color increased accordingly, with clockwise rotation (negative vorticity) shown in blue and counterclockwise rotation (positive vorticity) in red. Vorticity, expressed as vortex magnitude (s^{-1}), was used as a parameter to evaluate the intensity of local vortex flow; however, it does not directly represent the global macroscopic vortex structure. Total vorticity (s^{-1}) was defined as the sum of clockwise and counterclockwise vorticity.

Vorticity was analyzed on measurement planes that were first aligned with an anatomically defined midsagittal orientation and then carefully adjusted so that, in all cases, either the right or left foramen of Monro and the cerebral aqueduct could be visualized within a single plane.

Statistical analysis

Healthy volunteers were divided into two subgroups according to age at the time of MRI (<60 years and ≥60

years) to compare ventricular and ITA morphology. The Mann–Whitney–Wilcoxon test was used to compare HD patients and healthy volunteers aged ≥60 years, as well as healthy volunteers aged <60 versus those aged ≥60 years. To compare flow parameters between HD patients and healthy volunteers, we additionally constructed an age-matched healthy control subgroup by selecting healthy volunteers aged ≥72 years (n = 15). The HD group was then subdivided into two subgroups based on 4D flow MRI streamline and vorticity maps in the third ventricle: (1) "Hakim without flow," defined as patients in whom no organized intraventricular flow or paired vortices were identified, and (2) "Hakim with severe inflow," defined as patients showing pronounced reversed upward CSF inflow from the cerebral aqueduct into the third ventricle accompanied by formation of paired vortices. Vorticity and morphological parameters were compared among these three groups using the same nonparametric tests as described above. Total vorticity (s^{-1}) was classified into three categories based on its distribution: low (<6), middle (6–12.9), and high (≥13). The chi-square test was applied to compare categorical variables between groups. Associations between continuous variables were assessed using Pearson's correlation coefficient (r). A probability value of P <0.05 was considered statistically significant. All statistical analyses were performed using R (version 4.2.3; The R Foundation for Statistical Computing; http://www.R-project.org).

RESULTS

Clinical Characteristics

This study enrolled 83 patients (41 males and 42 females; mean age, 77.0 ± 6.2 years) diagnosed with HD (iNPH), and 226 healthy volunteers (85 males and 141 females, mean age: 58.2 ± 18.2 years) were included in this study. All ventricular volumes and volume ratios normalized to intracranial volume significantly differ between patients with HD and healthy volunteers aged ≥60 years, as well as between healthy volunteers aged <60 (younger group) and those aged ≥60 years (older group) (Table 1). All patients with HD exhibited the typical imaging feature of disproportionately enlarged subarachnoid space (DESH) [39-43].

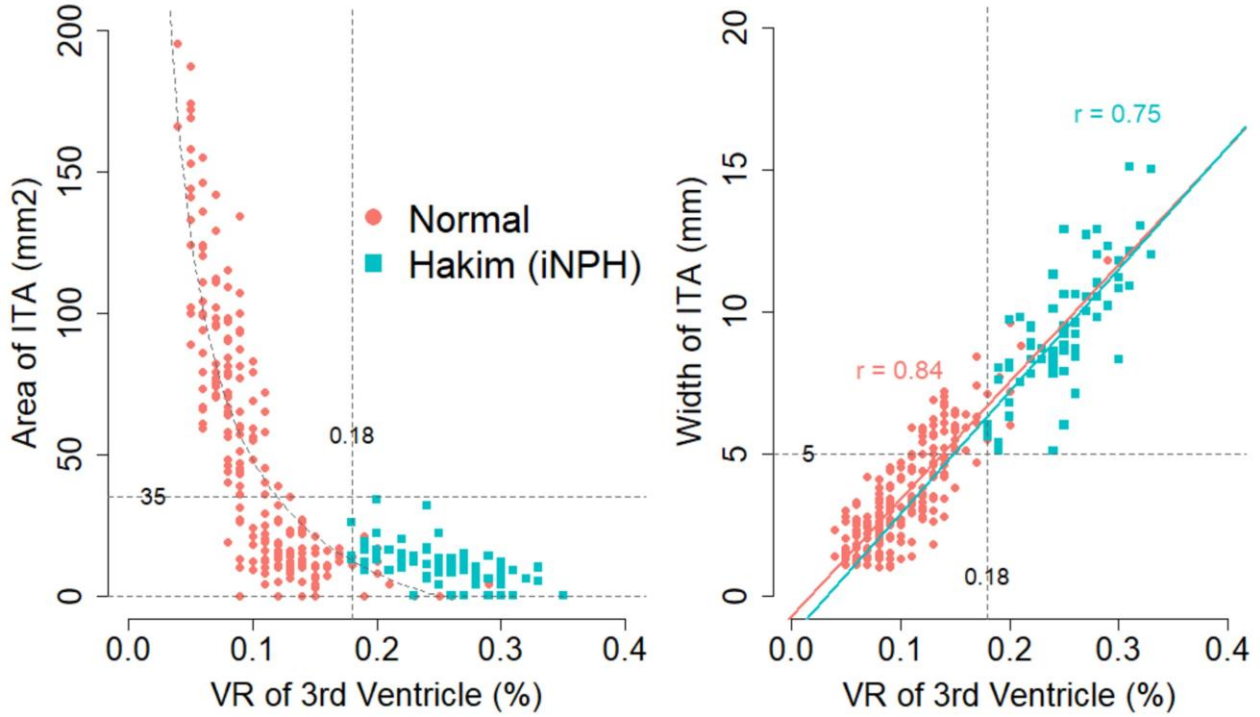

Figure 2. Relationship between third ventricular volume ratio and ITA area and width. Scatterplots showing the ratio of third ventricular volume to intracranial volume (X-axis) plotted against ITA area (left, Y-axis) and ITA width (right, Y-axis). Salmon-colored dots represent healthy volunteers, and cyan squares represent patients with Hakim's disease (iNPH). The ITA area showed an inverse relationship with the ventricular volume ratio; in patients with Hakim's disease, the ventricular volume ratio was ≥0.18% and the ITA area was <35 mm². The regression curve represents a reciprocal (hyperbolic) fit (ITA area = a / ventricular volume ratio + b) obtained by nonlinear least-squares fitting. In contrast, ITA width was linearly correlated with the ventricular volume ratio, with widths ≥5 mm in patients with Hakim's disease. Pearson's correlation coefficients (r) were 0.84 in healthy controls and 0.75 in patients, both indicating strong correlations.

Table 1. Clinical characteristics of the study population.

	Healthy volunteer				
	<60 years	60<= years	Hakim (iNPH)	P^1	P^2
Total number	95	131	83		
DESH	0	2	83	<0.001	0.624
Sex (male: female)	30:65	55:76	41:42	0.357	0.146
Mean age ± SD (years)	39.6 ± 11.4	71.6 ± 6.8	77.0 ± 6.2	<0.001	<0.001
Total CSF volume (mL)	301.2 ± 47.1	382.7 ± 61.8	438.5 ± 60.7	<0.001	<0.001
Total CSF volume ratio (%)	20.8 ± 2.5	26.7 ± 3.1	29.6 ± 2.4	<0.001	<0.001
Total ventricle volume (mL)	22.8 ± 7.8	38.8 ± 15.3	119.6 ± 31.8	<0.001	<0.001
Total ventricle volume ratio (%)	1.6 ± 0.5	2.7 ± 0.9	8.0 ± 1.8	<0.001	<0.001
Lateral ventricle volume (mL)	19.8 ± 7.4	35 ± 14.6	113.1 ± 31.1	<0.001	<0.001
Lateral ventricle volume ratio (%)	1.4 ± 0.5	2.4 ± 0.9	7.6 ± 1.8	<0.001	<0.001
Third ventricle volume (mL)	1.1 ± 0.4	1.8 ± 0.7	3.8 ± 0.8	<0.001	<0.001
Third ventricle volume ratio (%)	0.08 ± 0.02	0.13 ± 0.04	0.26 ± 0.04	<0.001	<0.001
Fourth ventricle volume (mL)	1.8 ± 0.3	2.0 ± 0.4	2.7 ± 0.7	<0.001	<0.001
Fourth ventricle volume ratio (%)	0.13 ± 0.01	0.14 ± 0.02	0.18 ± 0.04	<0.001	<0.001
Thalamic volume (mL)	14.6 ± 1.3	13.1 ± 1.2	13.1 ± 1.3	0.918	<0.001
Thalamic volume ratio (%)	1.0 ± 0.1	0.9 ± 0.1	0.9 ± 0.1	0.002	<0.001
Width of ITA (mm)	2.2 ± 1.0	4.5 ± 1.8	9.2 ± 2.3	<0.001	<0.001
Area of ITA (mm²)	84.1 ± 46.1	28.9 ± 26.6	10.5 ± 7.3	<0.001	<0.001
Max diameter of ITA (mm)	11.0 ± 3.7	6.2 ± 2.8	3.8 ± 1.3	<0.001	<0.001
Min diameter of ITA (mm)	7.5 ± 2.8	3.8 ± 2.5	1.9 ± 0.7	<0.001	<0.001
Area of Magendi's F.	12.7 ± 8.3	27.5 ± 15.6	43.6 ± 18.9	<0.001	<0.001
Diameter of Magendi's F.	3.0 ± 1.2	4.2 ± 1.9	6.7 ± 2.4	<0.001	<0.001

P^1: Probability value from the Mann–Whitney–Wilcoxon test comparing Hakim's disease (HD; iNPH) patients with healthy volunteers aged ≥60 years. P^2: Probability value from the Mann–Whitney–Wilcoxon test comparing healthy volunteers aged <60 years with those aged ≥60 years. Area of Magendie's F.: Cross-sectional area of the foramen of Magendi

Interthalamic Adhesion Morphology and Third Ventricle Size

The width and area of the ITA were significantly associated with the volume and volume ratio of the third ventricle (Fig. 2). As the third ventricle enlarged, ITA width increased linearly, with greater area and maximum diameter. As shown in Table 1, Compared with the healthy younger group (<60 years; mean ITA width 2.2 mm, mean ITA area 84.1 mm²), the healthy older group (≥60 years; 4.5 mm, 28.9 mm²) demonstrated a two-fold greater mean ITA width, while the mean ITA area was reduced to approximately 34% of that in the younger group. In patients with HD (mean ITA width 9.2 mm, mean ITA area 10.5 mm²), the mean width was approximately four times greater and the mean area was reduced to approximately 12% of the value observed in the healthy younger group.

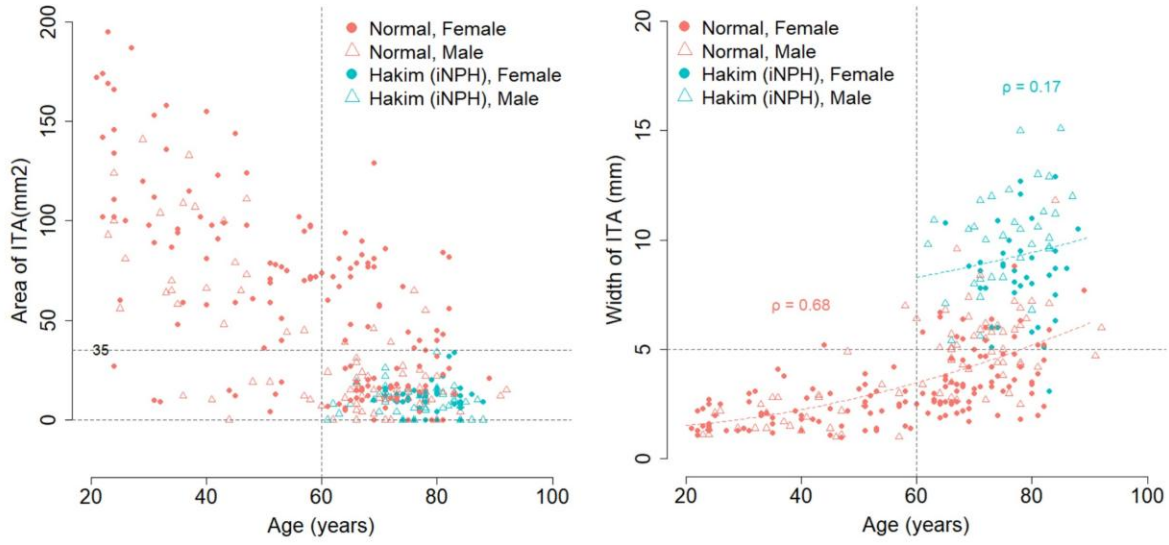

Figure 3. Relationship between age, sex, and ITA area and width. Scatterplots showing age (X-axis) plotted against ITA area (left, Y-axis) and ITA width (right, Y-axis). Salmon-colored symbols represent healthy volunteers and cyan symbols represent patients with Hakim's disease (iNPH). Circles indicate female subjects and triangles indicate male subjects. ITA area ranged widely from 0 (absence) to 200 mm². Larger areas were seen more frequently in younger individuals, whereas in those aged ≥60 years the area was generally ≤100 mm². In patients with Hakim's disease aged ≥60 years, ITA area was consistently <35 mm². Among healthy volunteers, ITA width tended to increase with age (Spearman's $\rho = 0.68$), with most individuals <60 years having widths <5 mm, whereas many ≥60-year-olds exceeded 5 mm. In patients with Hakim's disease, ITA width showed no correlation with age ($\rho = 0.17$), with a mean width of approximately 10 mm.

Although the maximum ITA area varied widely among individuals (0–200 mm²), it was generally larger in the younger group and decreased with aging (Fig. 3).

As shown in Figure 1C and Figure 4A–D. Reduction of the recess typically began in its superior half, and with progressive diminution, the upper portion disappeared, resulting in a rugby ball–like configuration consisting solely of the inferior portion (Fig. 1D and Supplementary Video 1). In the HD group, ITA area was consistently ≤35 mm² (Fig. 2).

Sex-stratified ITA measurements in healthy volunteers and patients with HD (iNPH) are summarized in Table 2. Among healthy volunteers <60 years, ITA width did not differ significantly between females and males (2.3 ± 0.9 mm vs 2.2 ± 1.3 mm, p = 0.434), whereas ITA area was larger in females (91.8 ± 47.0 mm²) than in males (67.3 ± 39.9 mm², p = 0.0255). In healthy volunteers aged ≧60 years, males showed greater ITA width (5.4 ± 1.8 mm vs 3.8 ± 1.6 mm, p < 0.0001) but smaller ITA area (16.6 ± 13.0 mm² vs 37.8 ± 30.3 mm², p < 0.0001), compared with females. In patients with HD, ITA width was also larger in males than in females (10.1 ± 2.3 mm vs 8.5 ± 2.1 mm, p = 0.004), whereas ITA area did not differ significantly between sexes (9.7 ± 7.4 mm² vs 11.4 ± 7.1 mm², p = 0.179).

Table 2. Interthalamic adhesion (ITA) width and area by sex in healthy volunteers and patients with Hakim's disease (HD).

	Female (n)	Male (n)	*P*
Healthy volunteer <60 years	65	30	
Width of ITA (mm)	2.3 ± 0.9	2.2 ± 1.3	0.434
Area of ITA (mm²)	91.8 ± 47.0	67.3 ± 39.9	0.0255
Healthy volunteer 60<= years	76	55	
Width of ITA (mm)	3.8 ± 1.6	5.4 ± 1.8	<0.001
Area of ITA (mm²)	37.8 ± 30.3	16.6 ± 13.0	<0.001
Hakim (iNPH)	42	41	
Width of ITA (mm)	8.5 ± 2.1	10.1 ± 2.3	0.004
Area of ITA (mm²)	11.4 ± 7.1	9.7 ± 7.4	0.179

P: Probability value from the Mann–Whitney–Wilcoxon test comparing females and males within each group.

Absence of the ITA was observed in one male (1%) in the younger group, nine individuals (7%, five males and four females) in the older group, and 12 individuals (14%, seven males and five females) in the HD group, without statistically significant differences (Table 3, Fig. 3). Although these results suggest that sex modulates ITA morphology, we could not identify a clear sex-related pattern that would explain the occurrence of HD.

CSF Dynamics in Third Ventricle

We assessed CSF dynamics in the third ventricle throughout one cardiac cycle using 4D Flow MRI. During systole, a continuous streamline of velocity vectors extended from the anterosuperior region near the foramen of Monro to the posteroinferior region near the cerebral aqueduct (Fig. 4, Supplementary Videos 2 and 3). In late diastole, small upward flow vectors emerged from the aqueduct into the third ventricle. These upward vectors, directed toward the ITA, divided into two rotational components: a clockwise vortex located posterior to the ITA and a counterclockwise vortex situated below the ITA and just above the midbrain. The counterclockwise vortex subsequently merged into the downward systolic streamline, while the clockwise vortex integrated into the aqueductal downward flow during systole.

Both the younger and older healthy groups, despite differences in ITA morphology, consistently exhibited this pattern: a long downward systolic streamline and a short upward diastolic streamline accompanied by paired vortices posterior to the ITA (Fig. 4, Supplementary Videos 2 and 3). As shown in Table 3, patients with HD were subdivided into two groups based on 4D flow MRI findings: a "Hakim without flow" group (n = 58), in whom no organized intraventricular flow or paired vortices were identified, and a "Hakim with severe inflow" group (n =

20), characterized by pronounced reversed upward CSF inflow from the cerebral aqueduct into the third ventricle with formation of paired vortices. These two HD subgroups were compared with an age-matched healthy control group (n = 15, ≥72 years).

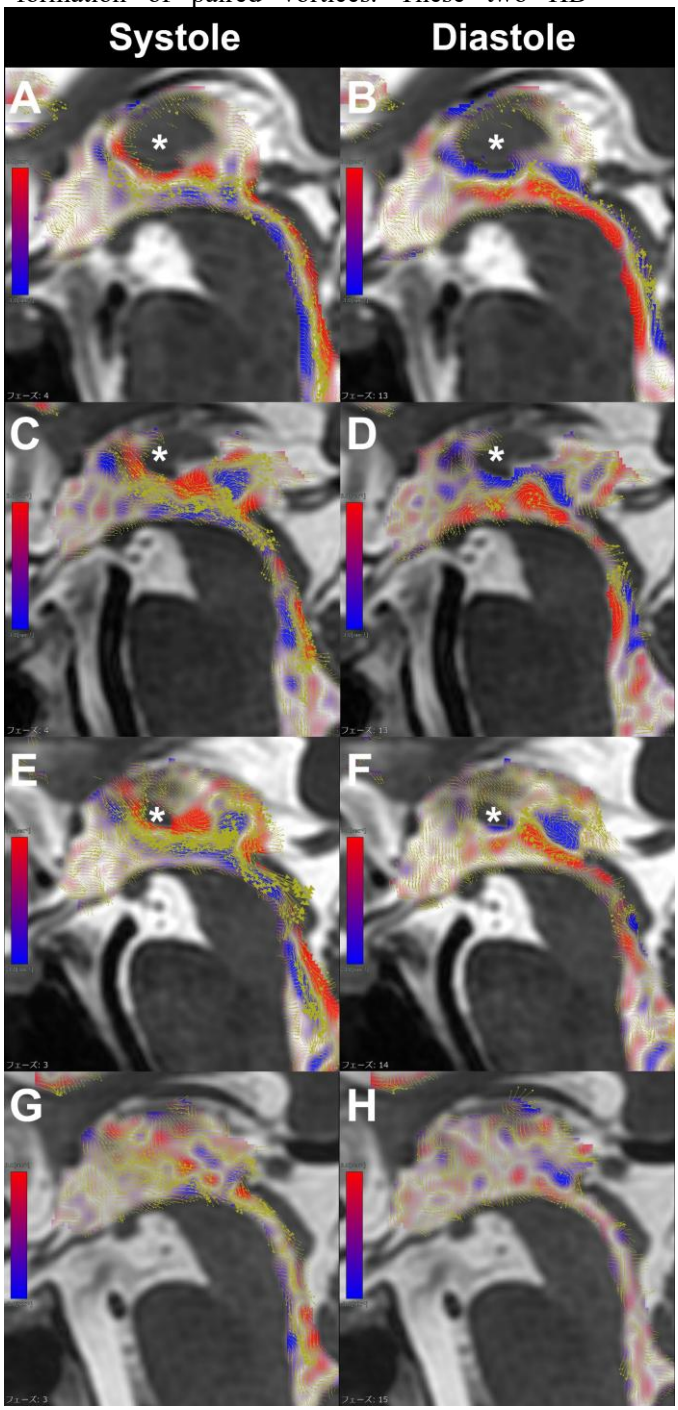

Figure 4. Vorticity maps in healthy volunteers. Vorticity maps of 2D sagittal views in healthy volunteers during the systolic phase (A, C, E, G) and diastolic phase (B, D, F, H). Clockwise vortices are shown in blue, counterclockwise vortices in red, and velocity vectors in yellow. The interthalamic adhesion (ITA, *) decreased in size in order (A, B) > (C, D) > (E, F) and was absent in (G, H). During diastole, counterclockwise vortices located just above the midbrain connected with the downward flow observed during systole. **(A** and **B)** Volunteer with the largest ITA, showing smooth downward and upward streamlines in the third ventricle. The ITA had a large posterior recess, where inflow from the cerebral aqueduct impinged and generated paired vortices. **(C** and **D)** Volunteer with a moderately sized ITA, exhibiting similar but slightly less organized streamlines. A prominent posterior recess behind the ITA was also observed, with aqueductal inflow contributing to vortex formation. **(E** and **F)** Volunteer with a small ITA, where diastolic inflow from the aqueduct generated paired vortices. However, the counterclockwise vortex (red) just above the midbrain showed weaker continuity with the systolic downward flow, resulting in a less smooth downward streamline from the foramen of Monro to the aqueduct. **(G** and **H)** Volunteer without an ITA, showing small paired vortices just anterior to the exit of the cerebral aqueduct.

Age and sex distributions did not differ significantly among the three groups. Consistent with the overall group comparisons, both HD subgroups showed greater ITA width, smaller ITA area, and larger foramen of Magendie area and diameter than age-matched controls, with no significant differences between the two HD subgroups. In patients in the "Hakim without flow" group, bidirectional streamlines within the third ventricle and paired vortices posterior to the ITA were absent (Fig. 5A–D, Supplementary Video 4). Instead, marked upward and downward vectors were confined to the cerebral aqueduct. Total vorticity in the third ventricle was significantly

lower in the "Hakim without flow" group than in age-matched controls, and these patients were most frequently classified as having low vorticity (64%). By contrast, in patients in the "Hakim with severe inflow" subgroup, large paired clockwise and counterclockwise vortices were observed within the third ventricle, generated by reverse upward flow from the aqueduct that extended to the roof of the ventricle and reached the foramina of Monro (Fig. 5E–H, Supplementary Video 5). This group showed higher mean total vorticity than the "Hakim without flow" group and did not differ significantly from age-matched controls. Notably, loss of a downward streamline in the third ventricle was observed in all patients in the "Hakim without flow" group, whereas downward streamlines were preserved in most patients in the "Hakim with severe inflow" group (75%) and in age-matched healthy controls (80%).

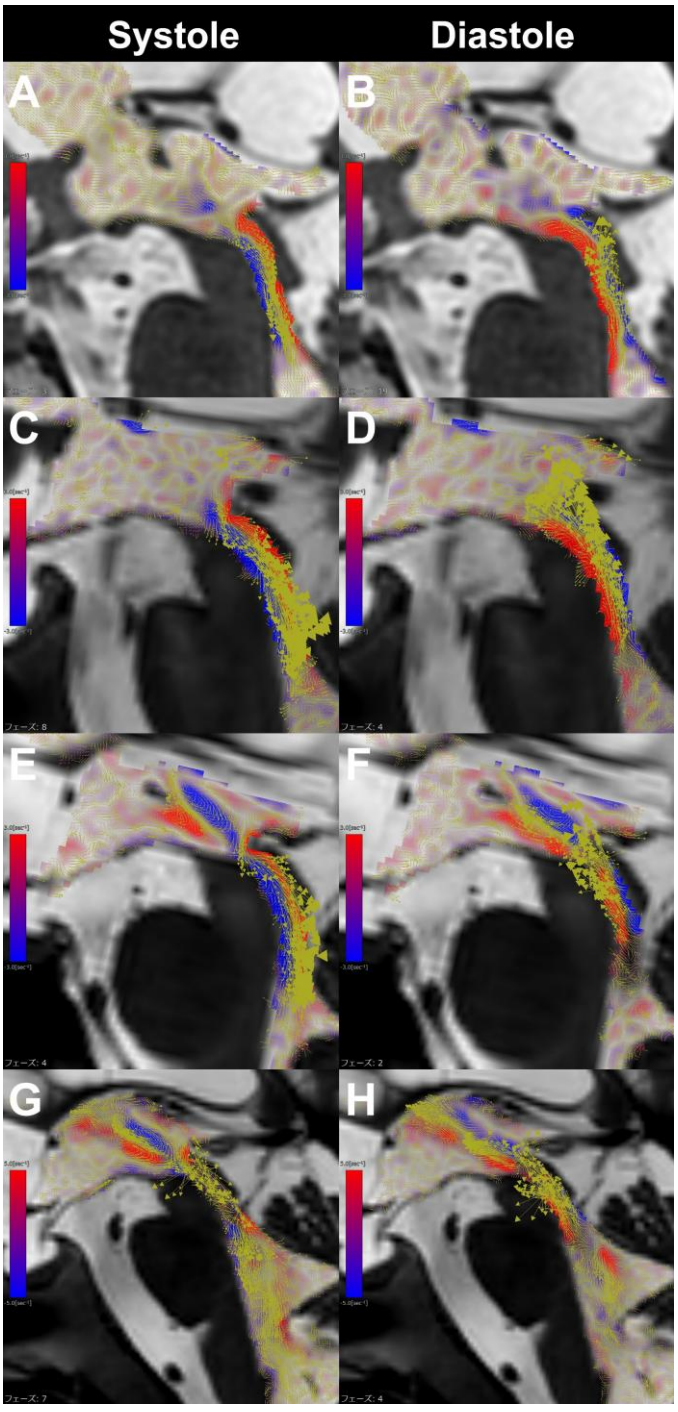

Figure 5. Vorticity maps in patients with Hakim's disease. Vorticity maps of 2D sagittal views in patients with Hakim's disease during the systolic phase (A, C, E, G) and diastolic phase (B, D, F, H). Clockwise vortices are shown in blue, counterclockwise vortices in red, and velocity vectors in yellow. **(A** and **B)** Patient with a small ITA, showing severe bidirectional aqueductal flow without third-ventricular flow or vortices. **(C** and **D)** Patient without an ITA, demonstrating a similar aqueductal flow pattern and absent third-ventricular dynamics. **(E** and **F)** Patient with a small ITA, exhibiting bidirectional aqueductal flow with large, paired vortices, clockwise (blue) and counterclockwise (red), posterior to the ITA. **(G** and **H)** Patient without an ITA, showing severe bidirectional aqueductal flow together with marked upward inflow extending to the roof of the third ventricle, generating paired vortices near the foramina of Monro.

In summary, both younger and older healthy groups exhibited physiological streamlines and vortices within the third ventricle. In HD, these organized flow patterns were either absent or markedly altered, and abnormal aqueductal inflow patterns predominated.

DISCUSSION

In this study, we demonstrated characteristic differences in ITA morphology and CSF dynamics of the third ventricle between healthy individuals and patients with HD (iNPH). Among healthy individuals, ITA area varied widely but tended to decrease with aging, and ITA width was significantly associated with the size of the third ventricle. Regarding normal CSF dynamics, irrespective of age, the third ventricle typically exhibited long downward systolic streamlines and short upward diastolic streamlines accompanied by paired vortices behind the ITA (Fig. 6). In contrast, these flow patterns were absent in patients with HD and were replaced by large abnormal bidirectional flows in the cerebral aqueduct. This observation is consistent with previous reports describing increased stroke volume in the cerebral aqueduct of patients with HD (iNPH), as measured by 2D phase-contrast MRI [44, 45] and 4D Flow MRI [21-23, 25]. However, those studies did not assess CSF dynamics within the third ventricle itself. Based on the abnormal bidirectional flow in the aqueduct, it had been assumed that the CSF within the third ventricle might also move in a chaotic and turbulent manner. However, our findings suggest a marked reduction in organized, large-scale circulatory flow within the third ventricle in patients with HD. Although vorticity was markedly reduced, this does not necessarily imply complete flow cessation. It is possible that disorganized or turbulent motion persists but fails to form coherent bidirectional flow or stable vortical structures. This interpretation aligns with the idea that our observations reflect a loss of organized large-scale circulation rather than true stagnation.

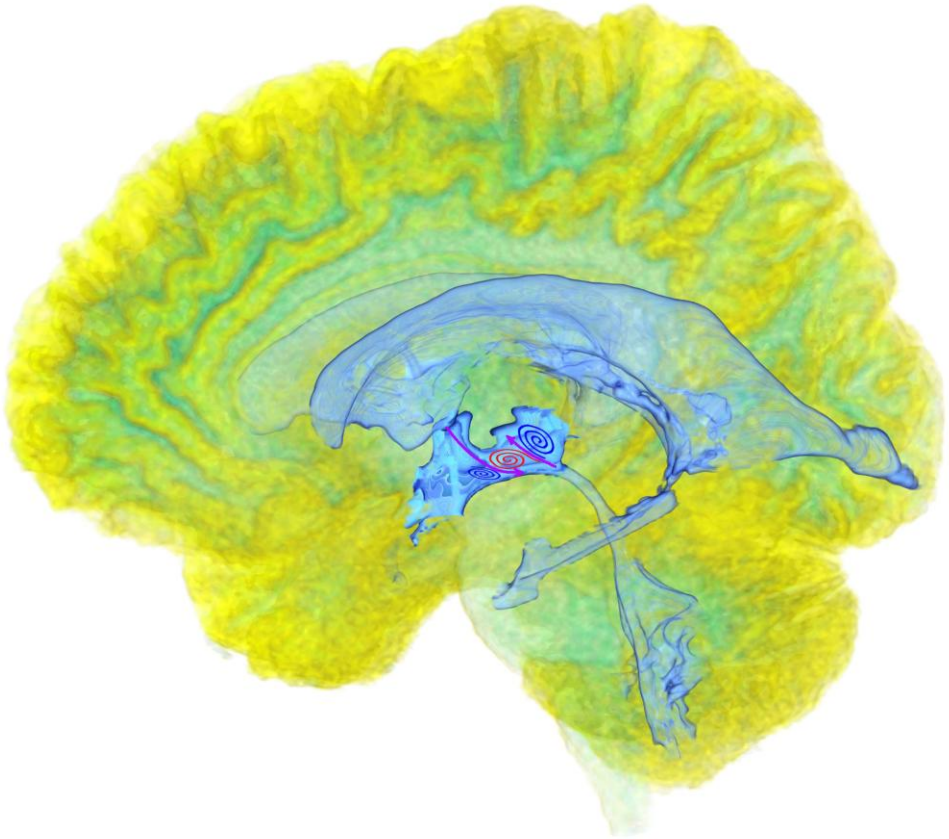

Figure 6. Normal cerebrospinal fluid dynamics in the third ventricle. In the central brain, cerebrospinal fluid enters the third ventricle through the bilateral foramina of Monro and the cerebral aqueduct. Behind the interthalamic adhesion, clockwise (blue) and counterclockwise (red) vortices arise, guiding these bidirectional inflows (purple) so that they do not collide, but merge into a smooth, synchronized circulation. This schematic serves as a conceptual summary of the organized, large-scale third-ventricular circulation observed in healthy subjects; in patients with Hakim's disease, such paired vortices and coherent bidirectional streamlines are no longer identifiable.

Although the functional role of the ITA has remained poorly understood [30], our findings suggest that it may contribute to maintaining third-ventricular geometry and organizing cardiac-synchronized CSF flow. The ITA is better regarded as one of several structural elements that limit lateral widening of the third ventricle and help buffer upward inflow from the cerebral aqueduct within it, thereby supporting the formation of paired vortices that, in turn, promote organized downward streamlines from the foramina of Monro toward the aqueduct. This conceptual shift allows the ITA to be regarded not merely as an anatomical variant, but as a potential modulator of ventricular CSF dynamics within the broader context of ventricular CSF dynamic failure in HD (iNPH).

We previously hypothesized that the earliest trigger of ventricular enlargement in HD (iNPH) is dilation of the foramina of Magendie and Luschka [46]. This hypothesis was based on our earlier findings that enlargement of the foramen of Magendie showed the strongest correlation with increased stroke volume in the cerebral aqueduct, and that aqueductal dilation was subsequently associated with increased stroke volume at the foramina of Monro [22]. When stroke volume in the cerebral aqueduct increases and strong CSF inflow enters the third ventricle, the ITA may act as a "second breakwater," preventing excessive transmission of this inflow directly toward the foramina of Monro.

In this study, approximately 75% of patients with HD (iNPH) showed no organized vortices or streamlines within the third ventricle, whereas the remaining 25% exhibited a distinct jet-like high-velocity inflow from the cerebral aqueduct into the third ventricle. We were unable to identify any definite anatomical or clinical factors that could explain this discrepancy. A cross-sectional study such as ours cannot capture longitudinal changes in CSF dynamics or in morphology, including that of the ITA and the third ventricle. Therefore, longitudinal prospective cohort studies that monitor temporal changes in third-ventricular morphology and CSF dynamics will be necessary to clarify the mechanisms underlying this currently unexplained divergence in flow patterns.

Patients with HD with an enlarged third ventricle also showed markedly smaller ITA area and markedly greater ITA width compared with healthy controls. These findings suggest that both morphological alterations of the ITA and changes in third-ventricular CSF dynamics may be closely linked to the pathophysiology of HD. The absence of physiological streamlines and vortices in the third ventricle may reflect impaired pulsatile CSF motion, thereby contributing to the loss of organized, cardiac-synchronized vortical flow and the development of clinical symptoms. In young healthy controls, the third ventricle was small and flattened, exhibiting clear heartbeat-synchronized bidirectional pulsatile CSF flow. By contrast, in HD, the third ventricle was markedly enlarged, and such organized pulsatile flow was absent. A plausible mechanism might be a phase mismatch between inflow from the foramen of Monro and from the cerebral aqueduct, which diminishes their normal buffering effect and results in disruption of organized, large-scale circulation within the third ventricle.

Significance of Vortex Flow in the Third Ventricle

Under normal conditions, continuous CSF circulation within the third ventricle is thought to play a crucial role in brain homeostasis (Fig. 6) [47]. These processes contribute to the regulation of the sleep–wake cycle and circadian rhythms through melatonin released from the pineal gland to the suprachiasmatic nuclei [10-13], as well as to neural cell regeneration in the subventricular zone [48, 49]. However, the impact of disrupted CSF circulation on brain disorders and sleep disturbances remains largely unknown. In HD, organized CSF flow in the third ventricle appears to be markedly impaired, which may interfere with hormone signaling and thereby contribute to sleep disturbances.

Proposal of a New Concept: Ventricular Failure

The term "ventricular failure" is well established in cardiology, where it refers to impaired contractile and pressure–volume function of the heart. Although the CSF system lacks direct mechanical parallels to cardiac physiology, we propose a conceptual adaptation of this term to describe chronic hydrocephalus as a condition in which CSF dynamics are persistently disturbed. In the present context, we use ventricular failure or dysfunction to denote a state in which the normal harmony of CSF dynamics in the third ventricle is disrupted. Adopting this conceptual definition may help classify previously unexplained forms of chronic hydrocephalus more clearly, thereby improving diagnostic accuracy and increasing confidence in treatment selection. Vortex hydrodynamics has been widely applied in cardiovascular research, serving as a key indicator of left ventricular dysfunction severity [14, 15, 26, 27]. By analogy at the level of flow patterns rather than mechanical properties, we suggest that the analysis of vortex structures in the third ventricle may provide new insights into ventricular dysfunction in hydrocephalus and potentially point toward novel therapeutic approaches. This framework introduces a new concept of true ventricular dysfunction based on CSF dynamics, complementing rather than replacing diagnosis that is currently grounded primarily in clinical outcomes.

This study has several limitations. First, the influence of respiration on CSF dynamics was not considered [21,

50-52]; future studies using respiration-gated 4D flow MRI ("5D flow") may help to quantify respiration-induced changes in vorticity throughout the CSF spaces [53]. Second, we did not evaluate the relationship between HD symptoms and CSF dynamics. Future studies should investigate associations between third-ventricular CSF dynamics and clinical features such as gait disturbance, cognitive impairment, and urinary dysfunction. Third, because this study had a cross-sectional design, causal relationships between morphological changes and CSF dynamics could not be established; this issue should be addressed in prospective cohort studies. Additional limitations include the potential selection bias in healthy volunteers, the limited spatiotemporal resolution of 4D flow MRI, and the lack of assessment of disease stage or postoperative changes in HD. In addition, all data were acquired on 3-T MRI systems from two different vendors at two institutes without formal harmonization, and 4D flow MRI was performed with different cardiac-phase sampling schemes (12 phases on the GE system and 8 phases on the Philips system). Thus, scanner-, site-, and protocol-related variability may have affected the morphological measurements and 4D flow–derived CSF dynamics, and temporal undersampling may have led to underestimation of peak velocities and vorticity. However, supplementary analyses examining scanner-related differences indicated that our principal findings were robust to these factors. A portion of the healthy volunteer dataset had been used in previous studies, which may also introduce sampling or selection bias, and the software module used for 4D flow analysis has not yet undergone external validation. Furthermore, vorticity was quantified on manually selected two-dimensional planes without blinding or repeated assessment, and interobserver reliability was not evaluated.

In conclusion, this study demonstrated marked differences in CSF dynamics within the third ventricle between healthy individuals and patients with HD (iNPH). In healthy individuals, heartbeat-synchronized streamlines and vortices were consistently observed, whereas in HD these physiological patterns were absent and replaced by abnormal bidirectional aqueductal flow. Based on 4D flow MRI with vorticity analysis, we propose the concept of ventricular CSF dynamics failure as a new framework for understanding chronic hydrocephalus.

Acknowledgments

We would like to thank the radiology staff of the Shiga University of Medical Science Hospital, Nagoya City University Hospital, and Rakuwakai Otowa Hospital. We also thank the FUJIFILM Corporation for using the latest version of SYNAPSE 3D workstation.

Supplementary Materials

The Supplementary data can be found online at: www.aginganddisease.org/EN/10.14336/AD.2025.1352.

References

[1] Iliff JJ, Wang M, Liao Y, Plogg BA, Peng W, Gundersen GA, et al. (2012). A paravascular pathway facilitates CSF flow through the brain parenchyma and the clearance of interstitial solutes, including amyloid beta. Sci Transl Med, 4:147ra111.

[2] Hablitz L, Nedergaard M (2024). Synchronized neuronal activity drives waste fluid flow. Nature, 627:44-45.

[3] Jiang-Xie LF, Drieu A, Bhasiin K, Quintero D, Smirnov I, Kipnis J (2024). Neuronal dynamics direct cerebrospinal fluid perfusion and brain clearance. Nature, 627:157-164.

[4] Keil SA, Jansson D, Braun M, Iliff JJ (2025). Glymphatic dysfunction in Alzheimer's disease: A critical appraisal. Science, 389:eadv8269.

[5] Louveau A, Smirnov I, Keyes TJ, Eccles JD, Rouhani SJ, Peske JD, et al. (2015). Structural and functional features of central nervous system lymphatic vessels. Nature, 523:337-341.

[6] Louveau A, Herz J, Alme MN (2018). CNS lymphatic drainage and neuroinflammation are regulated by meningeal lymphatic vasculature. Nature Neurosci, 21.

[7] Smyth LCD, Xu D, Okar SV, Dykstra T, Rustenhoven J, Papadopoulos Z, et al. (2024). Identification of direct connections between the dura and the brain. Nature, 627:165-173.

[8] Plog BA, Kim K, Verhaege D, Kim MW, Papadopoulos Z, Dikranian K, et al. (2025). A route for cerebrospinal fluid flow through leptomeningeal arterial-venous overlaps enables macromolecule and fluid shunting. Nat Neurosci, 28:1436-1445.

[9] Penzo MA, Robert V, Tucciarone J, De Bundel D, Wang M, Van Aelst L, et al. (2015). The paraventricular thalamus controls a central amygdala fear circuit. Nature, 519:455-459.

[10] Hassani OK, Lee MG, Jones BE (2009). Melanin-concentrating hormone neurons discharge in a reciprocal manner to orexin neurons across the sleep-wake cycle. Proc Natl Acad Sci U S A, 106:2418-2422.

[11] Kostin A, Alam MA, McGinty D, Alam MN (2021). Adult hypothalamic neurogenesis and sleep-wake dysfunction in aging. Sleep, 44.

[12] Myung J, Schmal C, Hong S, Tsukizawa Y, Rose P, Zhang Y, et al. (2018). The choroid plexus is an important circadian clock component. Nature Communications, 9.

[13] Reiter RJ, Tan DX, Kim SJ, Cruz MH (2014). Delivery of pineal melatonin to the brain and SCN: role of canaliculi, cerebrospinal fluid, tanycytes and Virchow-Robin perivascular spaces. Brain Struct Funct, 219:1873-1887.

[14] Kheradvar A, Rickers C, Morisawa D, Kim M, Hong GR, Pedrizzetti G (2019). Diagnostic and prognostic

significance of cardiovascular vortex formation. J Cardiol, 74:403-411.
[15] Sengupta PP, Pedrizetti G, Narula J (2012). Multiplanar visualization of blood flow using echocardiographic particle imaging velocimetry. JACC Cardiovasc Imaging, 5:566-569.
[16] Dandy WE, Blackfan KD (1964). Internal hydrocephalus: an experimental, clinical and pathological study. Journal of Neurosurgery, 21:588–635.
[17] Olstad EW, Ringers C, Hansen JN, Wens A, Brandt C, Wachten D, et al. (2019). Ciliary Beating Compartmentalizes Cerebrospinal Fluid Flow in the Brain and Regulates Ventricular Development. Curr Biol, 29:229-241 e226.
[18] Weed LH (1938). Meninges and Cerebrospinal Fluid. J Anat, 72:181-215.
[19] Kurtcuoglu V, Soellinger M, Summers P, Boomsma K, Poulikakos D, Boesiger P, et al. (2005). Reconstruction of cerebrospinal fluid flow in the third ventricle based on MRI data. Med Image Comput Comput Assist Interv, 8:786-793.
[20] Kurtcuoglu V, Soellinger M, Summers P, Boomsma K, Poulikakos D, Boesiger P, et al. (2007). Computational investigation of subject-specific cerebrospinal fluid flow in the third ventricle and aqueduct of Sylvius. J Biomech, 40:1235-1245.
[21] Rivera-Rivera LA, Vikner T, Eisenmenger L, Johnson SC, Johnson KM (2023). Four-dimensional flow MRI for quantitative assessment of cerebrospinal fluid dynamics: Status and opportunities. NMR Biomed:e5082.
[22] Yamada S, Ishikawa M, Ito H, Yamamoto K, Yamaguchi M, Oshima M, et al. (2020). Cerebrospinal fluid dynamics in idiopathic normal pressure hydrocephalus on four-dimensional flow imaging. Eur Radiol, 30:4454-4465.
[23] Yamada S, Ito H, Ishikawa M, Yamamoto K, Yamaguchi M, Oshima M, et al. (2021). Quantification of Oscillatory Shear Stress from Reciprocating CSF Motion on 4D Flow Imaging. AJNR Am J Neuroradiol, 42:479-486.
[24] Yamada S, Okada K, Ito H, Fujinami R, Yamanaka T, Yamada H, et al. (2025). Cerebrospinal Fluid Flow and Vorticity in Hydrocephalus on 4-Dimensional Flow MRI. Neurosurgery Practice, 6.
[25] Vikner T, Johnson KM, Cadman RV, Betthauser TJ, Wilson RE, Chin N, et al. (2024). CSF dynamics throughout the ventricular system using 4D flow MRI: associations to arterial pulsatility, ventricular volumes, and age. Fluids Barriers CNS, 21:68.
[26] Itatani K, Sekine T, Yamagishi M, Maeda Y, Higashitani N, Miyazaki S, et al. (2022). Hemodynamic Parameters for Cardiovascular System in 4D Flow MRI: Mathematical Definition and Clinical Applications. Magn Reson Med Sci, 21:380-399.
[27] Uribe S, Beerbaum P, Sorensen TS, Rasmusson A, Razavi R, Schaeffter T (2009). Four-dimensional (4D) flow of the whole heart and great vessels using real-time respiratory self-gating. Magn Reson Med, 62:984-992.
[28] Trzesniak C, Kempton MJ, Busatto GF, de Oliveira IR, Galvao-de Almeida A, Kambeitz J, et al. (2011). Adhesio interthalamica alterations in schizophrenia spectrum disorders: A systematic review and meta-analysis. Prog Neuropsychopharmacol Biol Psychiatry, 35:877-886.
[29] Vidal JP, Rachita K, Servais A, Peran P, Pariente J, Bonneville F, et al. (2024). Exploring the impact of the interthalamic adhesion on human cognition: insights from healthy subjects and thalamic stroke patients. J Neurol, 271:5985-5996.
[30] Parra JED, Ripoll AP, Garcia JFV (2022). Interthalamic adhesion in humans: a gray commissure? Anat Cell Biol, 55:109-112.
[31] Allen LS, Gorski RA (1991). Sexual dimorphism of the anterior commissure and massa intermedia of the human brain. J Comp Neurol, 312:97-104.
[32] Borghei A, Piracha A, Sani S (2021). Prevalence and anatomical characteristics of the human massa intermedia. Brain Struct Funct, 226:471-480.
[33] Damle NR, Ikuta T, John M, Peters BD, DeRosse P, Malhotra AK, et al. (2017). Relationship among interthalamic adhesion size, thalamic anatomy and neuropsychological functions in healthy volunteers. Brain Struct Funct, 222:2183-2192.
[34] Cheng S, Tan K, Bilston LE (2010). The effects of the interthalamic adhesion position on cerebrospinal fluid dynamics in the cerebral ventricles. J Biomech, 43:579-582.
[35] Tullberg M, Toma AK, Yamada S, Laurell K, Miyajima M, Watkins LD, et al. (2024). Classification of Chronic Hydrocephalus in Adults: A Systematic Review and Analysis. World Neurosurg, 183:113-122.
[36] Yamada S, Otani T, Ii S, Ito H, Iseki C, Tanikawa M, et al. (2024). Modeling cerebrospinal fluid dynamics across the entire intracranial space through integration of four-dimensional flow and intravoxel incoherent motion magnetic resonance imaging. Fluids Barriers CNS, 21:47.
[37] Yamada S, Yuzawa T, Ito H, Iseki C, Kondo T, Yamanaka T, et al. (2025). Regional Brain Volume Changes in Hakim's Disease vs. Alzheimer's and Mild Cognitive Impairment. Brain Communications, 7.
[38] Yavuz Ilik S, Otani T, Yamada S, Watanabe Y, Wada S (2022). A subject-specific assessment of measurement errors and their correction in cerebrospinal fluid velocity maps using 4D flow MRI. Magn Reson Med, 87:2412-2423.
[39] Hashimoto M, Ishikawa M, Mori E, Kuwana N (2010). Diagnosis of idiopathic normal pressure hydrocephalus is supported by MRI-based scheme: a prospective cohort study. Cerebrospinal Fluid Research, 7.
[40] Nakajima M, Yamada S, Miyajima M, Ishii K, Kuriyama N, Kazui H, et al. (2021). Guidelines for management of idiopathic normal pressure hydrocephalus (Third edition): Endorsed by the Japanese society of normal pressure hydrocephalus. Neurol Med Chir (Tokyo).
[41] Yamada S, Ito H, Matsumasa H, Tanikawa M, Ii S, Otani T, et al. (2023). Tightened Sulci in the High Convexities

as a Noteworthy Feature of Idiopathic Normal Pressure Hydrocephalus. World Neurosurg, 176:e427-e437.

[42] Yamada S, Ito H, Matsumasa H, Ii S, Otani T, Tanikawa M, et al. (2024). Automatic assessment of disproportionately enlarged subarachnoid-space hydrocephalus from 3D MRI using two deep learning models. Front Aging Neurosci, 16:1362637.

[43] Yamada S, Ito H, Matsumasa H, Ii S, Otani T, Tanikawa M, et al. (2024). Deep Learning Assessment of Disproportionately Enlarged Subarachnoid-Space Hydrocephalus in Hakim's Disease or Idiopathic Normal Pressure Hydrocephalus. Radiology Advances, 1.

[44] Shanks J, Markenroth Bloch K, Laurell K (2019). Aqueductal CSF stroke volume is increased in patients with idiopathic normal pressure hydrocephalus and decreases after shunt surgery. AJNR Am J Neuroradiol, 40.

[45] Bradley WG, Queralt SD (1996). Normal-pressure hydrocephalus: evaluation with cerebrospinal fluid flow measurements at MR imaging. Radiology, 198.

[46] Yamada S, Ishikawa M, Nozaki K (2021). Exploring mechanisms of ventricular enlargement in idiopathic normal pressure hydrocephalus: a role of cerebrospinal fluid dynamics and motile cilia. Fluids Barriers CNS, 18:20.

[47] Edelbo BL, Andreassen SN, Steffensen AB, MacAulay N (2023). Day-night fluctuations in choroid plexus transcriptomics and cerebrospinal fluid metabolomics. PNAS Nexus, 2:pgad262.

[48] Saunders NR, Dziegielewska KM, Fame RM, Lehtinen MK, Liddelow SA (2023). The choroid plexus: a missing link in our understanding of brain development and function. Physiol Rev, 103:919-956.

[49] Taranov A, Bedolla A, Iwasawa E, Brown FN, Baumgartner S, Fugate EM, et al. (2024). The choroid plexus maintains adult brain ventricles and subventricular zone neuroblast pool, which facilitates poststroke neurogenesis. Proc Natl Acad Sci U S A, 121:e2400213121.

[50] Chen L, Beckett A, Verma A, Feinberg DA (2015). Dynamics of respiratory and cardiac CSF motion revealed with real-time simultaneous multi-slice EPI velocity phase contrast imaging. Neuroimage, 122:281-287.

[51] Karki P, Murphy MC, Ganji S, Gunter JL, Graff-Radford J, Jones DT, et al. (2025). Real-Time 2D Phase-Contrast MRI to Assess Cardiac- and Respiratory-Driven CSF Movement in Normal Pressure Hydrocephalus. J Neuroimaging, 35:e70000.

[52] Liu P, Owashi K, Monnier H, Metanbou S, Capel C, Baledent O (2024). Validating the accuracy of real-time phase-contrast MRI and quantifying the effects of free breathing on cerebrospinal fluid dynamics. Fluids Barriers CNS, 21:25.

[53] Soderstrom P, Eklund A, Karalija N, Andersson BM, Riklund K, Backman L, et al. (2025). Respiratory influence on cerebral blood flow and blood volume - A 4D flow MRI study. J Cereb Blood Flow Metab, 45:1531-1542.